Lithium-Ion Conduction in a Class of Aluminoborates LinMAlB₁₂O₂₄

(M = Ba, Sr, Ca, or La; n = 7 or 6)

Yu Chen^{1,2}, Zijian Cai^{1,2}, Caleb Ramette³, Huiwen Ji^{3,*}

¹ Department of Materials Science and Engineering, University of California Berkeley, Berkeley, CA 94720, USA

² Materials Sciences Division, Lawrence Berkeley National Laboratory, Berkeley, CA 94720, USA

³ Department of Materials Science and Engineering, University of Utah, Salt Lake City, UT 84112, USA

*Corresponding author:

Prof. Huiwen Ji (Email: <u>huiwen.ji@utah.edu</u>)

Abstract

With diverse structures and high ambient stability, Li-containing borate materials are promising candidates as Li solid-state conductors. Here, we report a group of aluminoborate compounds, $\text{Li}_n\text{MAlB}_{12}\text{O}_{24}$ (n=6 for M=La; n=7 for M=Ba, Sr, Ca), which were synthesized by a conventional solid-state method. Their crystal structures feature a common three-dimensional framework consisting of $B_6\text{O}_{14}$ clusters and AlO₆ octahedra and the Li ions are positioned around the chained $B_6\text{O}_{14}$ clusters. The Li content n can be modified, i.e. either 6 or 7, depending on the chosen metal species M to keep the overall charge balance. The Li-ion conduction properties of the series were studied by bond valence site energy calculation and electrochemical impedance spectroscopy. We observed much higher ionic conductivity and a lower migration barrier in $\text{Li}_7\text{BaAlB}_{12}\text{O}_{24}$ than in $\text{Li}_6\text{LaAlB}_{12}\text{O}_{24}$, suggesting that the Li-ion site configuration plays an important role in determining ion transport.

KEYWORDS: Borate materials, solid-state ionic conductors, Li-ion conductivities, Li configuration

Introduction

A surge of academic and industrial interest in all-solid-state batteries (ASSBs), driven by the improved safety and higher energy density with the use of lithium (Li) metal anodes, has brought a class of materials known as superionic solid-state electrolytes (SSEs) to the forefront of battery research (1-3). SSEs with high ionic conductivity, low electrical conductivity, and excellent chemical/electrochemical stability are desired, to enable the use of both high-voltage cathodes and Li metal anodes (4). To date, numerous sulfide-based materials have been reported as SSEs (with ionic conductivity $\sigma > 0.1$ mS/cm). Several even show higher Li-ion conductivities, e.g., 25 mS/cm for $\text{Li}_{9.54}\text{Si}_{1.74}\text{P}_{1.44}\text{S}_{11.7}\text{Cl}_{0.3}$ (5) and 12 mS/cm for $\text{Li}_{10}\text{GeP}_2\text{S}_{12}$ (6), than those of liquid electrolytes, which is ~ 10 mS/cm. However, the narrow electrochemical stability windows and poor interfacial chemical stability of sulfides have limited their adoption as SSEs (7). In terms of stability, oxide materials are often superior to sulfides (8). However, high Li-ion conductivities were only achieved in a handful of oxide-based systems, which include the garnet-type (9), the NASICONtype (10), and the perovskite-type structures (11). In addition, these systems usually contain scarce or rare-earth elements such as La and Sc. Therefore, new families of Li-containing oxide solidstate materials of high stability and free from scarce metals are still needed.

Borate materials can be promising ionic conductors because of their low price, high ambient stability, wide electrochemical stability window, and remarkable structural flexibility. For these reasons, some Li-containing borates were recently suggested as coating materials for degradation mitigation of NMC-type cathodes (12, 13). Owing to the flexible B-O coordination environments (i.e. containing both BO₃ planar triangles and BO₄ tetrahedra), the structural chemistry of borates is extraordinarily diverse and complex with various types of polyanionic oxoboron clusters and connectivity (14), providing ample opportunities to yield favorable structures for ion migration.

Indeed, many borate-based crystalline and amorphous compounds have been reported to possess significant ionic mobility. Strauss *et al.* identified a high-temperature polymorph α-Li₆CuB₄O₁₀, which shows a high Li-ion conductivity of 2.7 mS cm⁻¹ at 350 °C. (15) Cakmak *et al.* proposed that partial F substitution for O can suppress the trapping effects of mobile ions at terminal positions in oxoborate materials and reported the first Li fluorooxoborate compound LiB₆O₉F as a potential solid-state ionic conductor (16). Following the strategy, Na₃B₃O₃F₆ and NaB₄O₆F were investigated as potential ionic conductors but showed very limited conductivities even at high temperature (17, 18). Li₄B₇O₁₂Cl was also reported to possess a high room-temperature ionic conductivity of 0.3 mS cm⁻¹ and remain stable up to 4.3 V vs. Li/Li⁺ (19). **Besides cationic mobility, borates have been recently reported as oxide ion conductors (20).**

In this work, we report a group of aluminoborates $\text{Li}_n\text{MAlB}_{12}\text{O}_{24}$ (n = 6 for M = La; n = 7 for M = Ba, Sr, Ca) as potential Li-ion solid-state conductors. Bond valence site energy (BVSE) calculations suggested a low Li migration barrier of 389 meV for three-dimensional (3D) Li-ion migration in $\text{Li}_7\text{BaAlB}_{12}\text{O}_{24}$ (which is referred to as "Ba-borate" hereafter). We then synthesized the $\text{Li}_7\text{MAlB}_{12}\text{O}_{24}$ series and studied their Li ion conductivities using electrochemical impedance spectroscopy (EIS). Furthermore, by substituting the divalent M with a trivalent metal cation, we successfully synthesized a new compound, $\text{Li}_6\text{LaAlB}_{12}\text{O}_{24}$ (referred to as "La-borate" hereafter), which shares a common framework structure but different Li site occupation. Comparing the conductivities of the Ba-borate and the La-borate, we revealed that the Li-ion site configuration has significant impact on ion conduction properties.

Experimental Methods

Synthesis of Li_nMAlB₁₂O₂₄: LiOH (Sigma-Aldrich, ≥ 98%), Ba(OH)₂·8H₂O (Sigma-Aldrich, ≥ 98%), Al(OH)₃ (Sigma-Aldrich), Sr(OH)₂·8H₂O (Sigma-Aldrich, ≥ 97%), Ca(OH)₂ (Sigma-Aldrich, 99.995%), La(OH)₃ (Sigma-Aldrich, 99.9%), H₃BO₃ (Sigma-Aldrich, ≥ 99.5%) were used as starting materials without further purification. For each composition, 3 grams of starting materials were weighed and transferred into a 50-mL zirconia jar. The precursors were mixed in ethanol using a Retsch PM200 planetary ball mill at 250 rpm for 12 hours. After ball milling, the precursors were dried overnight and pelletized. The precursor pellets (D 6mm) were wrapped in gold foils, placed in an alumina crucible, and sintered at high temperature in air. Specific details for each composition are as follows:

Li₇BaAlB₁₂O₂₄: LiOH (10% excess), Ba(OH)₂·8H₂O, Al(OH)₃ and H₃BO₃ were mixed in a stoichiometric ratio. The precursor pellets were first sintered overnight at 600 °C, followed by fine grinding, re-pelletizing, and re-sintering at 700 °C overnight. The same steps were repeated again at 750 °C to obtain the final product.

Li₇SrAlB₁₂O₂₄: LiOH (10% excess), Sr(OH)₂·8H₂O (3% excess), Al(OH)₃ and H₃BO₃ were mixed in a stoichiometric ratio. The precursor pellets were first sintered overnight at 600 °C, followed by fine grinding, re-pelletizing, and re-sintering at 700 °C overnight. The same steps were repeated again at 750 °C to obtain the final product.

Li₇CaAlB₁₂O₂₄: LiOH (10% excess), Ca(OH)₂, Al(OH)₃ and H₃BO₃ were mixed in a stoichiometric ratio. The precursor pellets were first sintered overnight at 600 °C, followed by fine grinding, re-pelletizing, and re-sintering at 700 °C overnight to obtain the final product.

Li₆LaAlB₁₂O₂₄: LiOH (10% excess), La(OH)₃ (20% deficient), Al(OH)₃ and H₃BO₃ were mixed in a stoichiometric ratio. The precursor pellets were first sintered overnight at 600 °C,

followed by fine grinding, re-pelletizing, and re-sintering at 750 °C overnight. The pellet was then ground again, ball-milled using a SpexSamplePrep 8000 M for 30 mininutes, re-pelletized, and resintered at 750 °C overnight to obtain the final product.

Structural Characterization: X-ray diffraction (XRD) of the as-synthesized Li₇MAlB₁₂O₂₄ (M = Ba, Sr, Ca) and Li₆LaAlB₁₂O₂₄ were obtained using a Rigaku MiniFlex 600 diffractometer equipped with a Cu source. The Lebail refinement of lattice parameters was performed using the HighScore Plus software package (21). Structure visualization was performed with VESTA (22). Scanning electron microscopy (SEM) images and energy dispersive X-ray spectroscopy (EDS) elemental mapping were obtained using a Phenom ParticleX Battery Desktop SEM (Thermo Fisher Scientific).

Electrochemical Impedance Spectroscopy (EIS): The sintered pellets (at ~80% relative density) were used for EIS measurements in Swagelok cells. Gold paste (Electron Microscopy Science) was applied to form ion-blocking electrodes. The room-temperature EIS measurements were conducted using a Bio-Logic VMP300 system in a frequency range of 7 MHz to 10 mHz with a 10 mV voltage amplitude. For variable-temperature EIS measurements, the Swagelok cell was placed into a tube furnace and connected to a Solartron MTS system. The impedance data at each temperature was collected after being stabilized for > 1 hour at the designated temperature, using an AC voltage of 10 mV amplitude from 1 MHz to 0.1 Hz. Data analysis was performed using the EC-Lab software package. The activation energy was determined from the slope of the Arrhenius plot.

Bond Valence Site Energy (BVSE) Calculation: Empirical BVSE calculation was performed using the SoftBV software tool (23). The crystal structure of Ba-borate used for BVSE calculation is the same as that reported in previous study (24).

Results and Discussion

The Li₇MAlB₁₂O₂₄ (M = Ba, Sr, Ca) series were first reported by Wei et al with structures determined from single-crystal X-ray diffraction refinements (24). These three compounds are isostructural with the same space group $R\overline{3}$. We will later show that the three exhibit similar ionic conductivities despite the widely varied M size from Ca²⁺ to Sr²⁺. Therefore, we will describe the Ba-borate in detail as a representative for the three. The crystal structure of the Ba-borate is shown in Figure 1a. It features a 3D- $[AlB_{12}O_{24}]_m^{9m}$ -framework that is composed of two types of building blocks, i.e. B₆O₁₄ clusters and AlO₆ octahedra, which are interconnected through vertex-sharing O atoms, as shown in Figure 1b. In Figure 1c, a 1D-B₆O₁₄ cluster chain running parallel to the c axis is isolated, which consists of BO₄ tetrahedra and BO₃ triangles in a 1:1 ratio and connected by O vertexes. The BO₃ planar triangles further act as bridges to connect the AlO₆ octahedra. The Ba atoms embedded in the structure are right above and below the Al atoms and are 12-coordinated. The Li sites as previously determined by single-crystal diffraction are either 5- or 6-coordinated and occupy two 18f Wyckoff positions (24), which are marked as Li1 and Li2 in Figure 1a, respectively. The Li1 site is fully occupied while the Li2 site is 1/6 occupied. The Li(1)O₅ and Li(2)O₆ polyhedra are connected through both edge- and face-sharing. As shown in Figure 1c, the Li1 and Li2 sites alternate around the B₆O₁₄ cluster chain, forming a unique Li helix configuration.

To explore whether Ba-borate has the potential to be a Li-ion solid-state conductor, we first calculated its 3D potential map of Li ions based on a bond valence site energy (BVSE) method, which has increasingly been applied as a screening tool for inorganic fast ion conductors (25, 26).

Specifically, pathways of low bond valence mismatch (i.e. hence energetically favorable) can be identified by sequentially placing the testing ion Li at all points in an entire unit cell. The site-energy iso-surfaces of Li ions are plotted in yellow in Figure 1d-1e, highlighting the simulated ion conduction paths. As shown in Figure 1d, along the *c* axis, the calculations suggest that Li ions move around the B₆O₁₄ cluster chain through the face-sharing or edge-sharing Li1 and Li2 sites, forming a helical-shaped migration pathway. The helices are further interconnected in the *ab* plane through nearby Li sites surrounding the AlO₆ octahedra, resulting in a 3D Li-ion conduction network (Figure 1e). Based on the BVSE calculation, the energy barrier for 3D Li-ion migration in the Ba-borate is 389 meV, which is comparable to some well-known Li superionic conductors (10, 27-29), suggesting that the Ba-borate is a promising candidate for solid-state Li conduction.

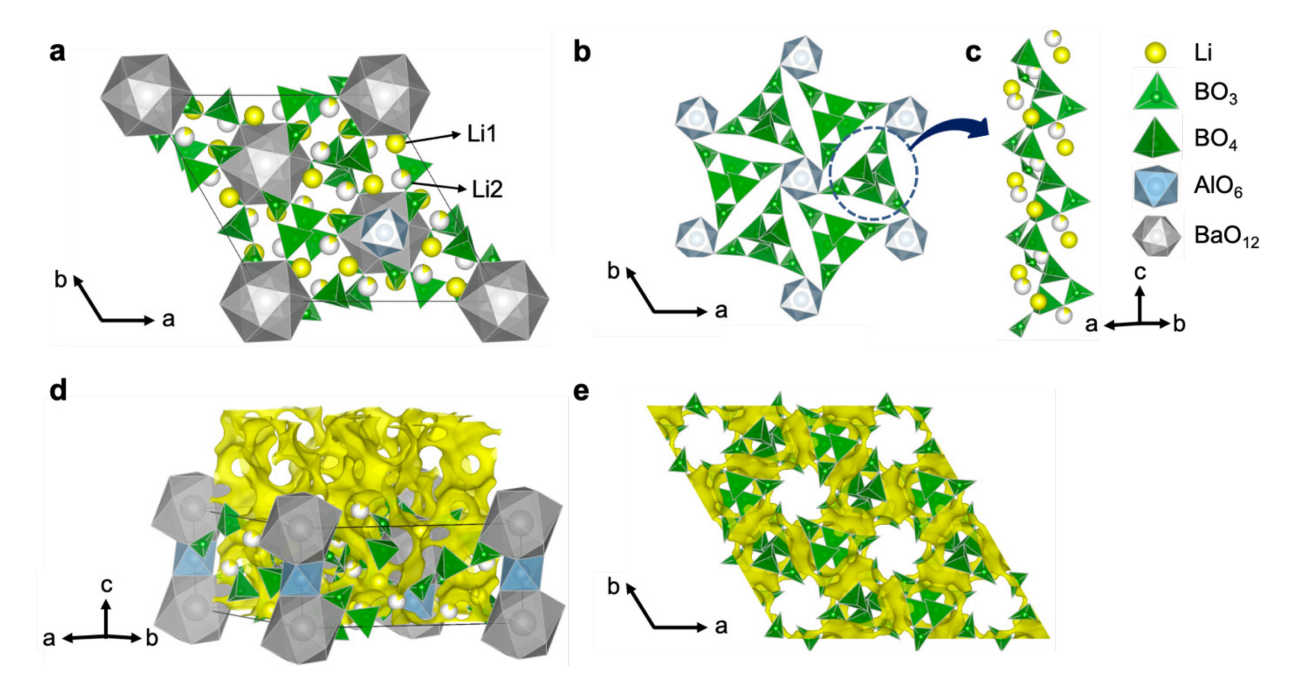


Figure 1. (a) Crystal structure of Ba-borate down the c axis. **(b)** View of the $[AlB_{12}O_{24}]_m^{9m}$ framework in Ba-borate down the c axis, in which the B_6O_{14} cluster chains are cross-linked by AlO_6 octahedra. **(c)** An isolated B_6O_{14} chain with nearby Li1 and Li2 sites. **(d-e)** Calculated Li potential map using a BVSE method, overlaid on the crystal structure. The yellow iso-surface of

constant BVSE highlights the simulated Li-ion conduction paths (iso-surface threshold, 0.98 eV over the global minimum).

The $Li_7MAlB_{12}O_{24}$ (M = Ba, Sr, Ca) series was previously synthesized by a hydrothermal method (24). Here, we used a solid-state synthesis method at 700–750 °C with metal hydroxides and boric acid as precursors. Due to the low melting points of the target phases (around 800 °C) and slow reaction kinetics of B₂O₃ that is a highly viscous medium, pure phases are very difficult to obtain. Multiple annealing steps were applied to obtain relatively high-purity samples. Subsequent structural characterization was carried out using powder X-ray diffraction (XRD), as shown in Figure 2a. The calculated Bragg positions for each phase are marked by vertical ticks. The XRD patterns of the Ba-borate, Li₇CaAlB₁₂O₂₄ (Ca-borate) and Li₇SrAlB₁₂O₂₄ (Sr-borate) show minor unknown impurities, which result in extra peaks between 20° and 30°. The background in these XRD patterns arises from the sample holder and the silicone grease underneath the powder. The LeBail-fitted lattice parameters are listed in Table 1. From the Baborate, the Sr-borate to the Ca-borate, the unit cell volume gradually decreases owing to the decreasing cation size from Ba²⁺, Sr²⁺ to Ca²⁺. Figure 2d presents the SEM image of Ba-borate powders and the corresponding EDS elemental mapping, which show a uniform distribution of B, O, and Al. Ba shows slight inhomogeneity, suggesting the existence of a small amount of Ba-rich impurity.

To further study the impact of Li content and Li site configuration on the ionic conductivity, we also synthesized a new compound, Li₆LaAlB₁₂O₂₄ (La-borate), by substituting trivalent La³⁺ for the divalent M cations. The XRD pattern of the as-synthesized La-borate showed exactly the same peak positions as the Ba-borate(Figure 2a, bottom), indicating that the main phase has the same 3D-[AlB₁₂O₂₄]_m^{9m}- framework as that in the Ba-borate. The refined lattice parameters of the

La-borate are also listed in Table 1 and its unit cell volume is even smaller than that of the Caborate, due to the comparable size of La³⁺ with Ca²⁺ yet a lower Li content per unit cell. **SEM** EDS elemental mapping shows a uniform distribution of B, O, Al, and La in La-borate (Figure 2e). Due to the aliovalent cation substitution, the Li content in the La-borate decreases from 7 to 6 to keep charge neutrality. In the Ba-borate with 7 Li/formula unit (f.u.), the Li1 site is fully occupied, corresponding to 6 Li/f.u.; whereas the Li2 site is only 1/6 occupied, corresponding to 1 Li/f.u., indicating that the Li1 site has lower site energy than Li2. Following the logic, in the La-borate with 6Li/f.u. in total, we expect that only the Li1 site shall be occupied in full, such that any short-distance Li-Li repulsion is removed and Li site energy is minimized. That is, Li ions only occupy the Li1 site while the Li2 site is empty, as shown in Figure 2b-2c. Indeed, in a previous study of isomorphic compounds $[Li_5A]SrAlB_{12}O_{24}$ (A = Mg, Zn) (30), it was reported that all the Li and A, at 6 ions/f.u., only occupy the Li1 site, confirming that this site is preferably occupied and directly corroborating our speculation. The removal of the Li2 site in the La-borate disrupts the otherwise helical-shaped Li site configuration observed in the Ba-borate and affects the Li-ion conduction in the host structure, which we will study and compare below.

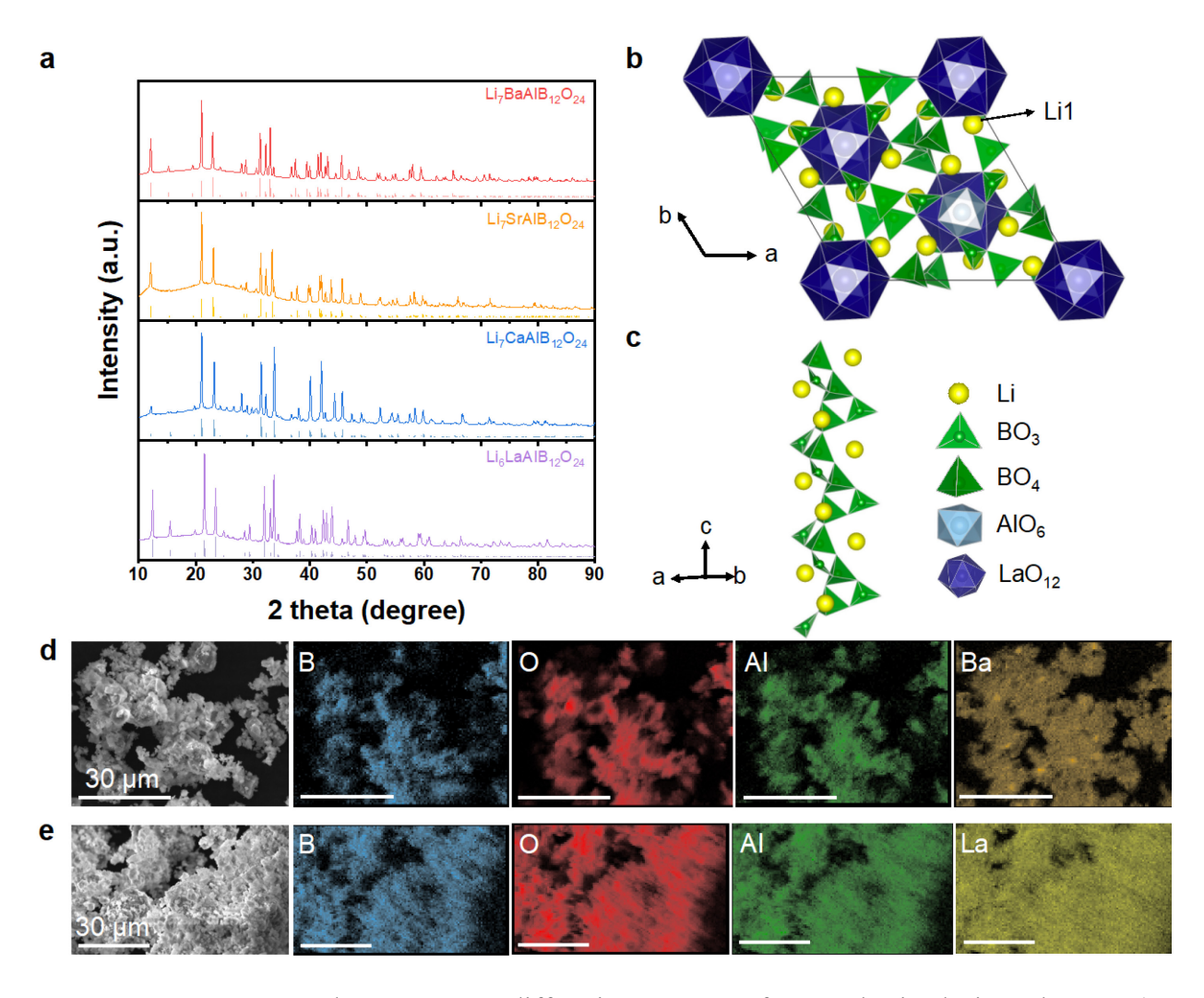


Figure 2. (a) From top to bottom, X-ray diffraction patterns of as-synthesized Li₇MAlB₁₂O₂₄ (M = Ba, Sr, Ca) and Li₆LaAlB₁₂O₂₄. Calculated Bragg positions are shown as vertical tick marks. **(b)** Crystal structure of La-borate viewed down the *c* axis. **(c)** View of an isolated B₆O₁₄-based cluster chain in La-borate with nearby Li1 sites. **(d)** SEM image of Ba-borate particles and corresponding EDS mapping. **(e)** SEM image of La-borate particles and corresponding EDS mapping.

Table 1. LeBail-fitted lattice parameters of Li₇MAlB₁₂O₂₄ (M = Ba, Sr, Ca) and Li₆LaAlB₁₂O₂₄.

	a (Å)	b (Å)	c (Å)	$V(Å^3)$
Li ₇ BaAlB ₁₂ O ₂₄	14.6884(10)	14.6884(10)	6.5773(5)	1228.93
Li ₇ SrAlB ₁₂ O ₂₄	14.6736(11)	14.6736(11)	6.4796(5)	1208.26
Li ₇ CaAlB ₁₂ O ₂₄	14.7129(13)	14.7129(13)	6.3994(6)	1199.69
$Li_6LaAlB_{12}O_{24}$	14.3619(13)	14.3619(13)	6.4740(6)	1156.47

The Li-ion conductivities in the Ba-borate, the Sr-borate, the Ca-borate, and the La-borate were determined on polycrystalline pellets by EIS using ion-blocking gold electrodes. Figure 3 presents the room-temperature Nyquist plots of the Ba-borate, the Ca-borate, and the Sr-borate. All impedance spectra feature a semicircle at high frequencies and a diffusion-limited linear tail at low frequencies. The data was fitted with an equivalent circuit consisting of two parallel constant phase elements (CPE, Q)/resistors (R) (for bulk and grain boundaries) in series with another CPE (for ion-blocking electrode capacitance). The fitting parameters are summarized in Table 2. The capacitances of CPEs obtained, around $10^{-12} \sim 10^{-11}$ F and $10^{-11} \sim 10^{-10}$ F for bulk and grain boundary capacitances, respectively, are typical for ionic conductors. (31) The obtained total ionic conductivity at room temperature is 1.45×10^{-7} S/cm for the Ba-borate, 1.35×10^{-7} S/cm for the Sr-borate, and 1.74×10^{-7} S/cm for the Ca-borate. These three compounds exhibit very similar Li-ion conductivities, which is consistent with their identical framework structure and Li content. Notably, these borates have excellent ambient stability. For example, the ionic conductivity of the Ba-borate as measured by EIS barely changes after 12-month exposure in air (Figure 3a).

The temperature-dependent Li conductivities of the Ba-borate exhibit Arrhenius behavior, as shown in Figure 4. The calculated energy barriers for Li ion migration in two different Ba-borate pellets are 548 ± 7 meV and 579 ± 14 meV, which are higher than the predicted migration barrier

by the BVSE method, 389 meV. The underestimation by the BVSE method is likely due to the fact that it ignores the interactions between mobile ions and its force field is simplified (23). The pre-factors $\log_{10} \sigma_0$ thus obtained are 4.76 ± 0.10 and 5.33 ± 0.22 , respectively.

For the La-borate, on the other hand, its ionic conductivity at room temperature is too low to be detected. EIS measurements were thus conducted in a high-temperature range from 220 to 380 °C. At 220 °C, La-borate shows a conductivity of 3.24×10^{-7} S/cm. An Arrhenius fitting of the variable temperature ionic conductivities yields an energy barrier of 772 ± 6 meV ($\log_{10}\sigma_0=4.11\pm0.05$) and 769 ± 6 meV ($\log_{10}\sigma_0=4.34\pm0.06$) in two La-borate pellets (Figure 4). If extrapolated to room temperature, the La-borate would have an ionic conductivity of $\sim 7.2\times10^{-12}$ S/cm. Therefore, despite the common framework structure, the Ba-borate has a much higher Li-ion conductivity and a much lower migration barrier than the La-borate, due to the different Li-ion configurations in these two compounds. The higher pre-factor of Ba-borate than that of Laborate is likely due to an increase of the effective charge carrier concentrations (32), consistent with the higher Li content in Ba-borate.

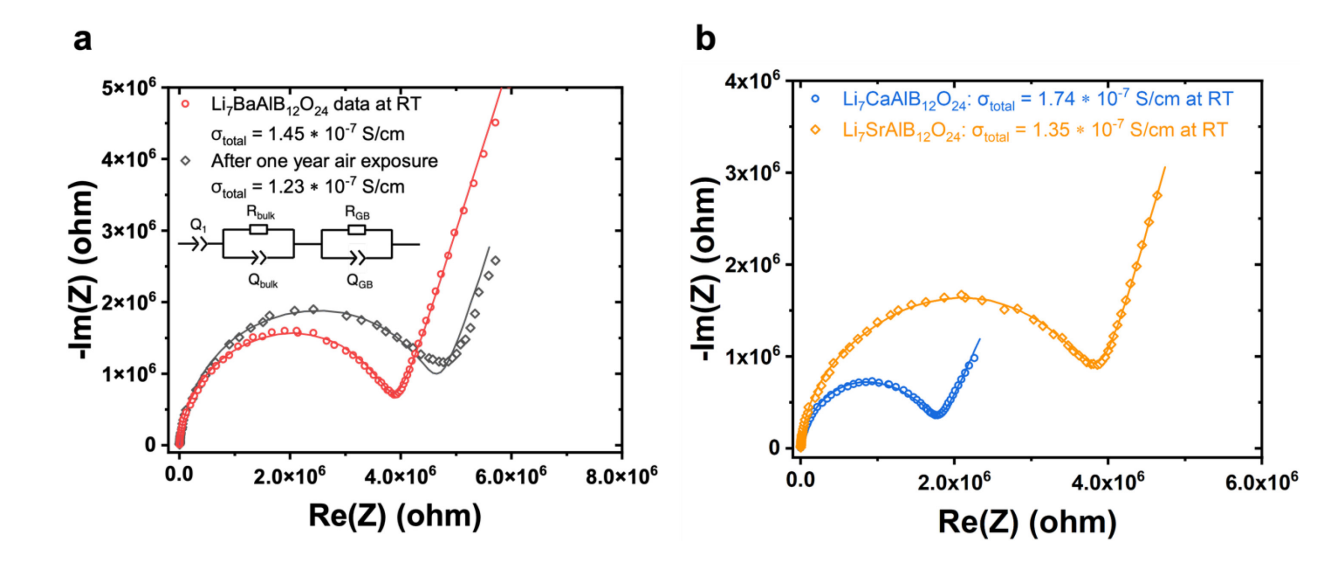


Figure 3. (a) Nyquist plot and the corresponding fit to an equivalent circuit for Ba-borate (red, circles), measured at room temperature under an ion-blocking condition on a freshly-made pellet. The equivalent circuit is displayed in the inset. Also shown is a Nyquist plot of the same pellet after one-year air exposure (black, diamonds). **(b)** Nyquist plots and the corresponding fits for Caborate (blue, circles) and Sr-borate (yellow, diamonds), measured at room temperature under an ion-blocking condition. The equivalent circuit used is the same as that in (a).

Table 2. The equivalent circuit fitting parameters for the analysis of EIS Nyquist plots.

Sample	Contribution	R (ohm)	C of CPE (F)	α of CPE	Total ionic conductivity (S/cm)	
Ba-borate	Bulk	1.02×10^6	6.74×10^{-12}	0.979		
	Grain boundary	2.79×10^6	1.75×10 ⁻¹¹	0.912	1.45×10 ⁻⁷	
	electrode	/	3.72×10 ⁻⁹	0.754]	
Ba-borate (1year air exposure)	Bulk	2.60×10^6	8.08×10 ⁻¹²	0.924		
	Grain boundary	1.89×10 ⁶	1.59×10 ⁻¹¹	1.00	1.22×10 ⁻⁷	
	electrode	/	2.65×10 ⁻⁹	0.751		
Ca-borate	Bulk	1.27×10^6	1.47×10 ⁻¹¹	0.924		
	Grain boundary	4.66×10 ⁵	2.21×10 ⁻¹⁰	0.872	1.76×10 ⁻⁷	
	electrode	/	8.98×10^{-9}	0.702		
Sr-borate	Bulk	6.12×10^5	6.92×10^{-12}	1.00		
	Grain boundary	3.16×10^6	1.23×10 ⁻¹¹	0.923	1.35×10 ⁻⁷	
	electrode	/	1.58×10 ⁻⁹	0.801		

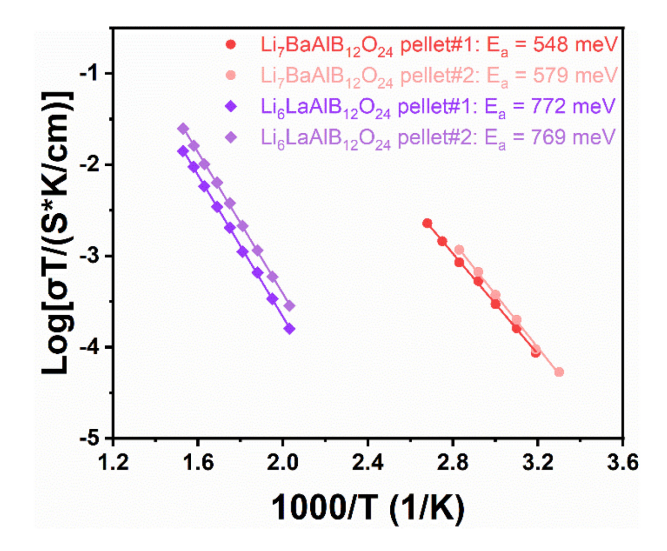


Figure 4. Arrhenius fits of ionic conductivities from variable-temperature EIS measurements for Ba-borate (red, circles) and La-borate (purple, diamonds). Two pellets were measured for every composition.

These aluminoborates thus constitute a new class of materials in which the Li configuration can be tuned by aliovalent M doping. The low-energy Li1 site can hold 6 Li/f.u.. Therefore, in the La-borate, Li ions would prefer only occupying the Li1 site such that the distances between nearby Li ions are maximized and their site energies are minimized. However, for the Ba-borate, full single-site occupation in Li1 cannot accommodate all 7 Li/f.u.. As a result, the additional Li ions have to occupy the Li2 site. Co-occupation of the Li1 and Li2 sites significantly decreases the distance between two adjacent Li ions from 4.268 Å to 2.09–2.45 Å, which leads to stronger Li-Li repulsion in Ba-borate than in La-borate where only Li1 site is occupied. The stronger Li-Li repulsion in Ba-borate might promote correlated Li-ion migration with a lower energy barrier, which is a mechanism suggested in several superionic conductors with high Li contents (33). Indeed, the BVSE calculations suggest that in the Ba-borate, Li ions migrate around the B₆O₁₄ cluster chain in helical-shaped Li1-Li2-Li1- pathways. In La-borate with only Li1 site occupation, although Li can still diffuse via the vacant Li2 site and interstitial sites, it lacks the strong Li-Li interactions and thus its Li diffusion mechanism might be different from that in Ba-borate. Therefore, even though the immobile framework of the Ba-borate and the La-borate remains the same, the different Li content and site occupation affects Li ion migration mechanism significantly, leading to the very different conduction properties observed in the two compounds. This work provides another example that a partially occupied Li sublattice caused by Li-stuffing promotes Li-ion diffusion. This effect has recently been reported in several other systems such as the Li garnets (34), a lithium titanate Li₄Ti₅O₁₂ anode with fast charging kinetics (35), and the Li argyrodites (36).

Although the Li ion conductivities in Li₇MAlB₁₂O₂₄ (M = Ba, Sr, Ca) are not comparable to several state-of-the-art Li superionic conductors, which typically have conductivities $> 10^{-4}$ S/cm

at room temperature and a migration barrier < 400 meV (1), these compounds have excellent air stability as observed in general for many borates (13). These aluminoborates are thus promising candidates as coating materials for high-voltage Li cathodes in ASSBs, to prevent undesired reactions between cathode and solid-state electrolyte, especially in the case where sulfide-based electrolytes are used.

Conclusion

In summary, we successfully synthesized a group of aluminoborate materials, Li₇MAlB₁₂O₂₄ (M = Ba, Sr, Ca) and Li₆LaAlB₁₂O₂₄ using a conventional solid-state method. Bond valence site energy calculations predicted that Li₇BaAlB₁₂O₂₄ has 3D Li-ion migration pathways with a low energy barrier of 389 meV. Our measured migration barrier for polycrystalline Li₇BaAlB₁₂O₂₄ is about 550 meV and its ionic conductivity at room temperature is 1.45×10⁻⁷ S/cm, comparable to Li₇SrAlB₁₂O₂₄ and Li₇CaAlB₁₂O₂₄. By substituting La³⁺ for the divalent cations, the change of Li site occupation in Li₆LaAlB₁₂O₂₄ leads to much poorer ion conduction, suggesting the important role of Li-ion site configuration in determining ionic conductivities. Though the conductivity of Li₇BaAlB₁₂O₂₄ is still lower than many superionic conductors, it is a promising candidate as cathode coating materials in all-solid-state batteries due to its excellent ambient stability.

Acknowledgements

This work is supported by National Science Foundation (DMR-2145832). C. R. and H. J. also acknowledge the startup support from the University of Utah.

References

- 1. Z. Zhang, Y. Shao, B. Lotsch, Y.-S. Hu, H. Li, J. Janek, L. F. Nazar, C.-W. Nan, J. Maier, M. Armand and L. Chen, *Energy & Environmental Science*, **11**, 1945 (2018).
- 2. J. Janek and W. G. Zeier, *Nature Energy*, **1**, 16141 (2016).
- 3. A. Manthiram, X. Yu and S. Wang, *Nature Reviews Materials*, **2**, 16103 (2017).
- 4. Q. Zhao, S. Stalin, C.-Z. Zhao and L. A. Archer, *Nature Reviews Materials*, **5**, 229 (2020).
- 5. Y. Kato, S. Hori, T. Saito, K. Suzuki, M. Hirayama, A. Mitsui, M. Yonemura, H. Iba and R. Kanno, *Nature Energy*, **1**, 16030 (2016).
- 6. N. Kamaya, K. Homma, Y. Yamakawa, M. Hirayama, R. Kanno, M. Yonemura, T. Kamiyama, Y. Kato, S. Hama, K. Kawamoto and A. Mitsui, *Nature Materials*, **10**, 682 (2011).
- 7. W. D. Richards, L. J. Miara, Y. Wang, J. C. Kim and G. Ceder, *Chemistry of Materials*, **28**, 266 (2016).
- 8. K. J. Kim, M. Balaish, M. Wadaguchi, L. Kong and J. L. M. Rupp, *Advanced Energy Materials*, **11**, 2002689 (2020).
- 9. C. Wang, K. Fu, S. P. Kammampata, D. W. McOwen, A. J. Samson, L. Zhang, G. T. Hitz, A. M. Nolan, E. D. Wachsman, Y. Mo, V. Thangadurai and L. Hu, *Chemical Reviews*, **120**, 4257 (2020).
- 10. H. Aono, E. Sugimoto, Y. Sadaoka, N. Imanaka and G. y. Adachi, *Journal of the electrochemical society*, **137**, 1023 (1990).
- 11. G.-y. Adachi, N. Imanaka and S. Tamura, *Chemical Reviews*, **102**, 2405 (2002).
- 12. Y. Xiao, L. J. Miara, Y. Wang and G. Ceder, *Joule*, **3**, 1252 (2019).
- 13. Y. Q. Zhang, Y. Tian, Y. Xiao, L. J. Miara, Y. Aihara, T. Tsujimura, T. Shi, M. Scott and G. Ceder, *Advanced Energy Materials*, **10**, 1903778 (2020).
- 14. M. A. Beckett, Coordination Chemistry Reviews, 323, 2 (2016).
- 15. F. Strauss, G. Rousse, D. Alves Dalla Corte, C. Giacobbe, R. Dominko and J.-M. Tarascon, *Inorganic Chemistry*, **57**, 11646 (2018).
- 16. G. Cakmak, J. Nuss and M. Jansen, *Zeitschrift für anorganische und allgemeine Chemie*, **635**, 631 (2009).
- 17. G. Cakmak, T. Pilz and M. Jansen, *Zeitschrift für anorganische und allgemeine Chemie*, **638**, 1411 (2012).
- 18. Z. Zhang, Y. Wang, B. Zhang, Z. Yang and S. Pan, *Angewandte Chemie International Edition*, **57**, 6577 (2018).
- 19. D. Tan, F. Wang, T. Pietsch, M. A. Grasser, T. Doert and M. Ruck, *ACS Applied Energy Materials*, **2**, 5140 (2019).
- 20. X. Li, L. Yang, Z. Zhu, X. Wang, P. Chen, S. Huang, X. Wei, G. Cai, P. Manuel, S. Yang, J. Lin, X. Kuang and J. Sun, *Science China Materials*, **65**, 2737 (2022).
- 21. T. Degen, M. Sadki, E. Bron, U. König and G. Nénert, *Powder Diffraction*, **29**, S13 (2014).
- 22. K. Momma and F. Izumi, *Journal of applied crystallography*, **44**, 1272 (2011).
- 23. H. Chen, L. L. Wong and S. Adams, *Acta Crystallographica Section B: Structural Science, Crystal Engineering and Materials*, **75** (2019).
- 24. Q. Wei, S. J. Sun, J. Zhang and G. Y. Yang, Chemistry—A European Journal, 23, 7614 (2017).
- 25. M. Avdeev, M. Sale, S. Adams and R. P. Rao, Solid State Ionics, 225, 43 (2012).
- 26. S. Adams and J. Swenson, *Solid State Ionics*, **154-155**, 151 (2002).

- 27. T. Asano, A. Sakai, S. Ouchi, M. Sakaida, A. Miyazaki and S. Hasegawa, *Advanced Materials*, **30**, 1803075 (2018).
- 28. L. Zhou, A. Assoud, A. Shyamsunder, A. Huq, Q. Zhang, P. Hartmann, J. Kulisch and L. F. Nazar, *Chemistry of Materials* (2019).
- 29. R. Murugan, V. Thangadurai and W. Weppner, *Angewandte Chemie International Edition*, **46**, 7778 (2007).
- 30. H. Song, N. Wang, X. Jiang, Y. Fu, Y. Li, W. Liu, Z. Lin, J. Yao and G. Zhang, *Inorganic chemistry*, **58**, 1016 (2018).
- 31. J. T. S. Irvine, D. C. Sinclair and A. R. West, *Advanced Materials*, **2**, 132 (1990).
- 32. B. Gadermaier, B. Stanje, A. Wilkening, I. Hanzu, P. Heitjans and H. M. R. Wilkening, *The Journal of Physical Chemistry C*, **123**, 10153 (2019).
- 33. X. He, Y. Zhu and Y. Mo, *Nature Communications*, **8**, 15893 (2017).
- 34. M. Xu, M. S. Park, J. M. Lee, T. Y. Kim, Y. S. Park and E. Ma, *Physical Review B*, **85**, 052301 (2012).
- 35. W. Schmidt, P. Bottke, M. Sternad, P. Gollob, V. Hennige and M. Wilkening, *Chemistry of Materials*, **27**, 1740 (2015).
- 36. K. Hogrefe, N. Minafra, I. Hanghofer, A. Banik, W. G. Zeier and H. M. R. Wilkening, *Journal of the American Chemical Society* (2022).